13th International Symposium on Particle Image Velocimetry – ISPIV 2019
Munich, Germany, July 22-24, 2019

On Subsonic Near-Wake Flows of a Space Launcher Configuration with Various Base Geometries

Dominik Saile*, Viktor Kühl, Ali Gülhan

DLR German Aerospace Center, Institute of Aerodynamics and Flow Technology, Supersonic and Hypersonic Technology Department, Cologne, Germany

* Dominik.Saile@dlr.de

Abstract

Buffet/buffeting as load imposing mechanism on the base structures of space launcher has been of strong interest ever since it was found as partially responsible for the failure flight 157 of Ariane 5. Several studies suggested that the base region is most excited at Mach 0.8. A preceding study of the current series on base flow effects revealed a differing excitation in comparison to the other subsonic Mach number cases. It featured an especially pronounced excitation in the recirculation region. Thus, the current work attempts to answer the question why this case appears to be distinct. This is done by decreasing the relative nozzle length and focusing on the Reynolds stress distribution. The research question is approached by experiments in the *Vertical Test Section Cologne (VMK)* on a base rocket model with supersonic, over-expanded exhaust jet exposed to an ambient flow at Mach 0.8 and a Reynolds number of $1.4 \cdot 10^6$. Data is acquired by means of *particle image velocimetry (PIV)*. The results reveal that a most unfavorable configuration appears to exist, which is if the mean shear layer reattachment takes place just on the tip of the nozzle.

1 Introduction

Buffet/buffeting as load imposing mechanism on the base structures of space launcher has been of strong interest ever since it was found as partially responsible for the failure flight 157 of Ariane 5. Buffet circumscribes the excitation of aerodynamic forces in the wake and buffeting the structural response. In resonance, the interaction between aerodynamic and structure loads can have disastrous consequences. The studies of David and Radulovic (2005); Schwane (2015) have found that flow conditions are especially detrimental for Ariane 5 in the transonic flow regime, in particular, at Mach 0.8.

The failure flight has triggered many studies to improve and extend the understanding of base flow phenomena. Investigations on similar base geometry representations for Ariane 5 have been conducted by Wong et al. (2007); Schrijer et al. (2011); Hannemann et al. (2011); Schwane (2015). On generic space launcher configurations, the governing mechanisms for buffeting have been analyzed among others by Fuchs et al. (1979), Deprés et al. (2004), Deck and Thorigny (2007), Weiss et al. (2009), Weiss and Deck (2013), Schrijer et al. (2014), Scharnowski (2013), Scharnowski et al. (2015), Scharnowski et al. (2016), Statnikov et al. (2016), Statnikov et al. (2017), van Gent et al. (2017b), and van Gent et al. (2017a). Statnikov et al. (2017) extended existing knowledge about governing mechanisms by means of *dynamic mode decomposition* and isolated three different modes of excitation in the base region: *cross-pumping* of the separation bubble and *cross-flapping* and *swinging* of the shear layer.

Few of the references above are experimental and even fewer with a supersonic exhaust jet (Deprés et al., 2004; Weiss and Deck, 2013; van Gent et al., 2017b), meaning there is generally a lack experimental data for validation. However, van Gent et al. (2017b) actually conducted a study which is comparable to the study at hand, but with a different focus. They found that for similar overall conditions (geometry+flow conditions) *'neither an increase in nozzle length nor the presence of an exhaust plume was found to lead to a significant change in the mean reattachment length'*. Further, it was concluded that the plume *'cannot accurately be modeled by replacing the plume with a solid geometry'*.

The first statement cannot be generally supported by the predecessor studies of the current work. A comparison between the *jet-off*- (Saile et al., 2019b) and *jet-on*-case (Saile et al., 2019a) shows clear differences when the jet is turned on. There, this was attributed to a base suction effect as previously described by Schoones and Bannink (1998); Deprés et al. (2004); Wolf (2013). The latter statement though can be

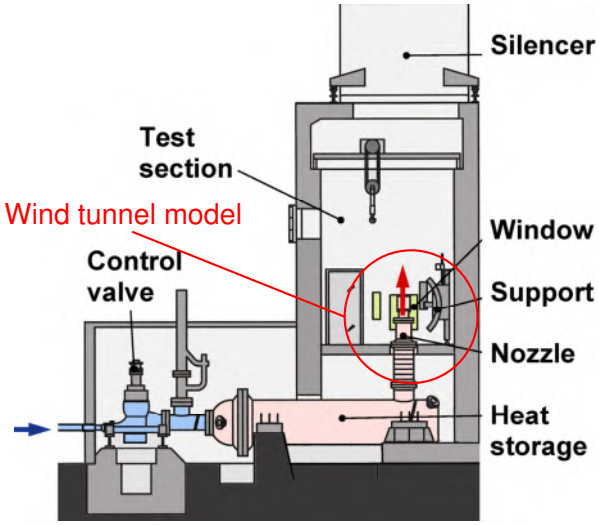

Figure 1: Schematic sketch of the VMK facility. The location of the wind tunnel model is encircled (in red) and the details of which are given in Fig. 2.

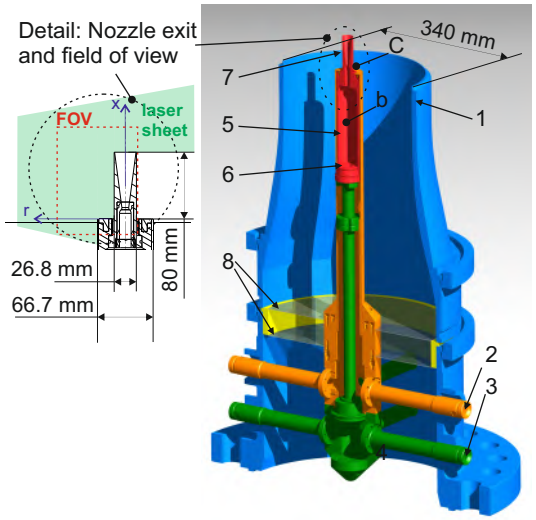

Figure 2: Sketch of the wind tunnel model with the wind tunnel nozzle (blue), cold jet supply system (green) and the chamber (red). The location in the frame of the facility is given in Fig. 1. The graph further shows the field of view (FOV).

supported by one of the predecessor studies. Saile et al. (2019a) found an unexpectedly strong excitation in the near-wake region at Mach 0.8, which is the motivation for the current work. The questions are as following:

- *How does this unexpected excitation react to a nozzle length change?*
- *Is it possible to identify the reason for this unexpected excitation?*

Thus, the objective here is to study the dependency of the space launcher to different relative nozzle lengths. More generally, the overarching idea is to provide data to the community as contribution for the development of further design guidelines for space launchers.

As in the previous studies of this series (Saile et al., 2019b,a), this task is approached by conducting experiments in the VMK on a base model representing generic space launcher configurations. The base model geometry is modified from test to test by changing the nozzle length. Experiments are executed at Mach 0.8 for a Reynolds number of $1.4 \cdot 10^6$. Data is captured by means of *particle image velocimetry (PIV)*, and the results mainly concern the mean and turbulent quantities for the velocity. To underline some points in the course of the discussion, the *probability density function (PDF)* of a point just upstream of the nozzle exit and selected instantaneous velocity distributions are shown.

The paper is structured as following: Hereafter in Ch. 2, the methods for data acquisition and analysis are presented followed by the description of the results in Ch. 3. A conclusion and outlook is given in Ch. 4.

2 Methods

VMK (Triesch and Krohn, 1986; DLR, 2019; Saile et al., 2015), sketched in Fig. 1, is a blow-down type wind tunnel featuring a vertical free test section for tests in the subsonic to supersonic range starting from Mach 0.5 up to 3.2. The current experiments were conducted with a subsonic nozzle featuring an exit diameter of 340 mm.

The baseline wind tunnel model integrated in the subsonic wind tunnel nozzle is sketched in Fig. 2. The main component of this base representation of a space launcher configuration is a cylindrical main body with a cylindrical nozzle attached to its base. The first has a diameter of $D = 66.7$ mm, the second of $d = 26.8$ mm. The smaller cylinder features a length of $L = 80$ mm. The geometry mimics the main generic

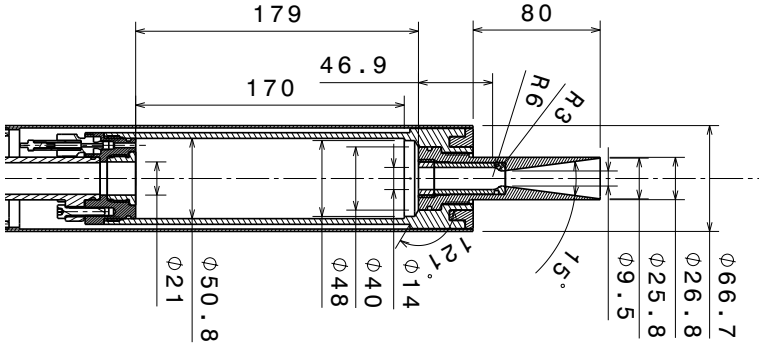

Figure 3: Technical drawing focusing on the chamber and nozzle geometry. Units are given in millimeter.

components of the Ariane 5 base with respect to its scaling ($d/D \sim 0.4$, $L/D \sim 1.2$). Further, the base plate is 10.4 mm downstream from the wind tunnel nozzle exit.

The baseline model described above is modified by attaching adapters of various lengths to the base. The adapters are cylindrical bodies with the outer diameter of the main body and an opening with the diameter of the nozzle. The adapters essentially reduce the relative nozzle length. Base adapters to generate the following additional relative nozzle lengths have been applied: $L/D = 0.45$, 0.6, 0.75, 0.9 and 1.05.

The nozzle remains the same for all base geometries. It has a conical contour and to avoid the occurrence of condensed oxygen in the cold exhaust jet, it was chosen to limit the expansion ratio to $\varepsilon = 7.37$, which is equivalent to a nozzle exit Mach number of 3.59 for an isentropic expansion of air.

Upstream of the wind tunnel nozzle exit (Fig. 2), the wind tunnel nozzle (1) is equipped with support arms (2) and (3), which have three tasks: First, they keep the wind tunnel model in place, second, one or several supports can be used as access point for the harnessing of the sensors, and third, one support is used for the air supply. The support arms converge in a central mounting (4) on top of which is the combustion or reservoir chamber (5). The injector (6) and the nozzle (7) are exchangeable to realize various injection conditions and nozzle exit conditions, respectively. The wind tunnel nozzle is equipped with two levels of straighteners (8) downstream of the support arms to reduce perturbations.

The results of the previous study (Saile et al., 2019b) revealed that the Mach 0.8-case poses a limiting case for the $L/D = 1.2$-configuration where base vortex region temporally exhibits a common interface with the jet. Consequently, the investigation is restricted an ambient flow equal to Mach 0.8. The details of the ambient flow are listed in Tab. 1, which are the exit Mach number Ma_C, exit velocity U_C, exit Reynolds number Re_C based on the diameter of the main cylinder. Additionally, the chamber pressure $p_{0,b}$ and temperature $T_{0,b}$ of the wind tunnel model are listed. The exit Mach number was calculated under the assumption of an isentropic expansion by means of the reservoir and ambient pressure; the velocity is directly taken from the PIV results. Due to corrupted results just upstream in the vicinity of the base separation point, the ambient flow (Tab. 1) was determined farther downstream from the base. The ambient flow is averaged over an area between $0.15 < x/D < 0.2$ and $0.7 < r/D < 0.8$.

The preceding studies additionally provide data of the incoming boundary layer for Mach 0.8 and a relative nozzle length of $L/D = 1.2$. Since only adapters have been added to the base of the space launcher configuration, it is assumed that the changes regarding the incoming boundary layer are negligible. For more details, please refer to Ref. (Saile et al., 2019b,a).

The PIV measurement setup features a minor difference regarding the field of view (FOV), but other than that, the setup was kept just as in Saile et al. (2019a), meaning a classical 2D-2C setup was used. The light sheet is generated with an *Ultra CFR Nd:YAG* laser system of *Big Sky Laser*. Each laser pulse contains 190 mJ at a wavelength of 532 nm. The sheet thickness was in the range of 0.5 mm. Perpendicular to the laser sheet, a *PCO*1600 camera system by *PCO AG* was set up at a distance of about 200 mm for the acquisition of the particle images. The *LabSmith* timing unit by *LC880* controls the trigger pulses for both components with an accuracy of 100 ps. The camera was equipped with the *Makro-Planar 2/35 ZF* lens by *Carl Zeiss AG*. The FOV to capture a global view of the wake is kept comparable to the one used in Saile et al. (2019a). It resolves about $134 \times 100\,\mathrm{mm}^2$. To accommodate for the base geometry adaptation, the FOVs are equally shifted downstream with increasing base adapter lengths. Due to the high depth of focus, the choice for the aperture setting has turned out to be unfortunate. The wind tunnel

Table 1: Free-stream conditions and reservoir conditions of the wind tunnel model

Run ID	L/D [-]	Ma_C [-]	U_C $[ms^{-1}]$	Re_C [-]	$p_{0,b}$ $[MPa]$	$T_{0,b}$ $[K]$	$[x_{vc}, r_{vc}]/D$ [-]
V163	1.2	0.79	257.5	$1.4 \cdot 10^6$	3.31	286.1	[0.48,0.35]
V196	1.05	0.80	263.4	$1.4 \cdot 10^6$	3.22	287.7	[0.58,0.36]
V191	0.9	0.79	261.5	$1.4 \cdot 10^6$	3.25	289.2	[0.47,0.36]
V195	0.75	0.80	261.6	$1.4 \cdot 10^6$	3.23	286.5	[0.5,0.36]
V177	0.6	0.79	265.1	$1.4 \cdot 10^6$	3.23	282.4	[0.56,0.36]
V198	0.45	0.79	265.7	$1.4 \cdot 10^6$	3.22	287.2	[0.53,0.36]

nozzle is faintly visible in the background of the raw images for occasionally weak seeding. For this reason, results are not discussed in that flawed range, meaning if they are located upstream from $x/D < 0.15$ and related to the incoming freestream ($r/D > 0.5$). The FOV for the relative nozzle length $L/D = 1.2$ is exemplarily depicted in Fig. 2, which also shows the coordinate system originating in the symmetry axis on the base. Seeding was accomplished with an in-house developed seeding generator providing titanium dioxide particles. Titanium dioxide of the type *K*1002 from *Kronos International, Inc.* was used, which exhibits according to the manufacturer a number based average diameter and density of $d_p = 0.23\,\mu$m and $\rho_p = 3800 kgm^{-3}$, respectively. The particles were injected into the flow at position 'A' (Fig. 2). The jet was not seeded.

The analysis of the images was executed with *PIVview V3.60* by *PIVTEC GmbH*. The relative motion between camera and wind tunnel model is negligible for this FOV and was consequently not corrected. The selection the setting of image sampling is based on the experience and results of the preceding study without jet (Saile et al., 2019b). In total, a number of 345 images per run were evaluated with a window size of $32 \times 16\,\text{px}^2$ with an overlap of $4 \times 4\,\text{px}^2$. In physical units, one interrogation window without overlap has a size of $2.68 \times 1.34\,\text{mm}^2$ (V163). The multi-grid interrogation method with grid refinement was applied, the *Whittaker* reconstruction (Raffel et al., 2007) was used for the sub-pixel peak fit and on the final pass, a B-spline interpolation scheme of 3^{rd} order was applied to cover the aspect of adaptive image deformation. The data was not interpolated.

An uncertainty analysis has been executed which is based on an approach suggested by Lazar et al. (2010). The analysis takes into account the equipment-related uncertainty, the uncertainty due to the particle lag and the sampling uncertainty. The equipment-related uncertainty includes calibration and timing error. The approach for the calculation of the sampling uncertainty is extracted from Benedict and Gould (1996). The total uncertainty for the field of view FOV amounts to $\pm 3.0\%$ with respect to the incoming flow velocity U_C. Further, the results have been checked for peak-locking, which in consequence was ruled out, and with respect to the signal-to-noise ratio.

3 Results & Discussion

Next, the response of the mean flow field to nozzle length alterations is presented. Afterwards, in Ch. 3.2, the focus is on the corresponding Reynolds stress fields. Then, in Ch. 3.3, the maxima of the Reynolds shear stress are extracted. In Ch. 3.4, an attempt is made to associate this previously found dependency of the Reynolds shear stress on the nozzle length to specific flow features. Last, hypotheses are discussed in Ch. 3.5.

3.1 Mean Velocity Distribution

The impact of the nozzle length variation on the mean velocity distribution is assessed in the following. The contour plots shown in Fig. 4 reveal that the reattachment process undergoes a significant change with decreasing nozzle length. As already seen in Saile et al. (2019a), the ambient flow starts to interact with the exhaust jet at about Mach 0.8 for the *Ariane 5*-like configuration with a nozzle length of $L/D = 1.2$. Obviously, this tendency is intensified for shorter nozzle lengths. As indicator here for the reattachment or starting point for interactions with the jet, one can use the stagnation streamline and the low speed corridor spreading up- and downstream from the vortex center (exemplarily marked with a dashed arrow for the

$L/D = 1.2$-case). Note that these are mean velocity quantities, which consequently do not reflect a possible temporary shear layer reattachment on the jet as it also takes place for the $L/D = 1.2$-configuration.

As stated above, for $L/D = 1.2$, reattachment predominantly takes place on the solid nozzle wall. For 1.05, the stagnation streamline and the low speed corridor move closer to the tip of the nozzle and coincide with it for $L/D = 0.9$. Then, for $L/D \leq 0.75$, an overhang of the mean recirculation bubble can be noticed. The mean axial flow in that region reverses while the stagnation streamline evolving from the shoulder of the base still anchors at the nozzle tip. In the area of jet influence, the ambient flow experiences a realignment and acceleration in the streamwise direction.

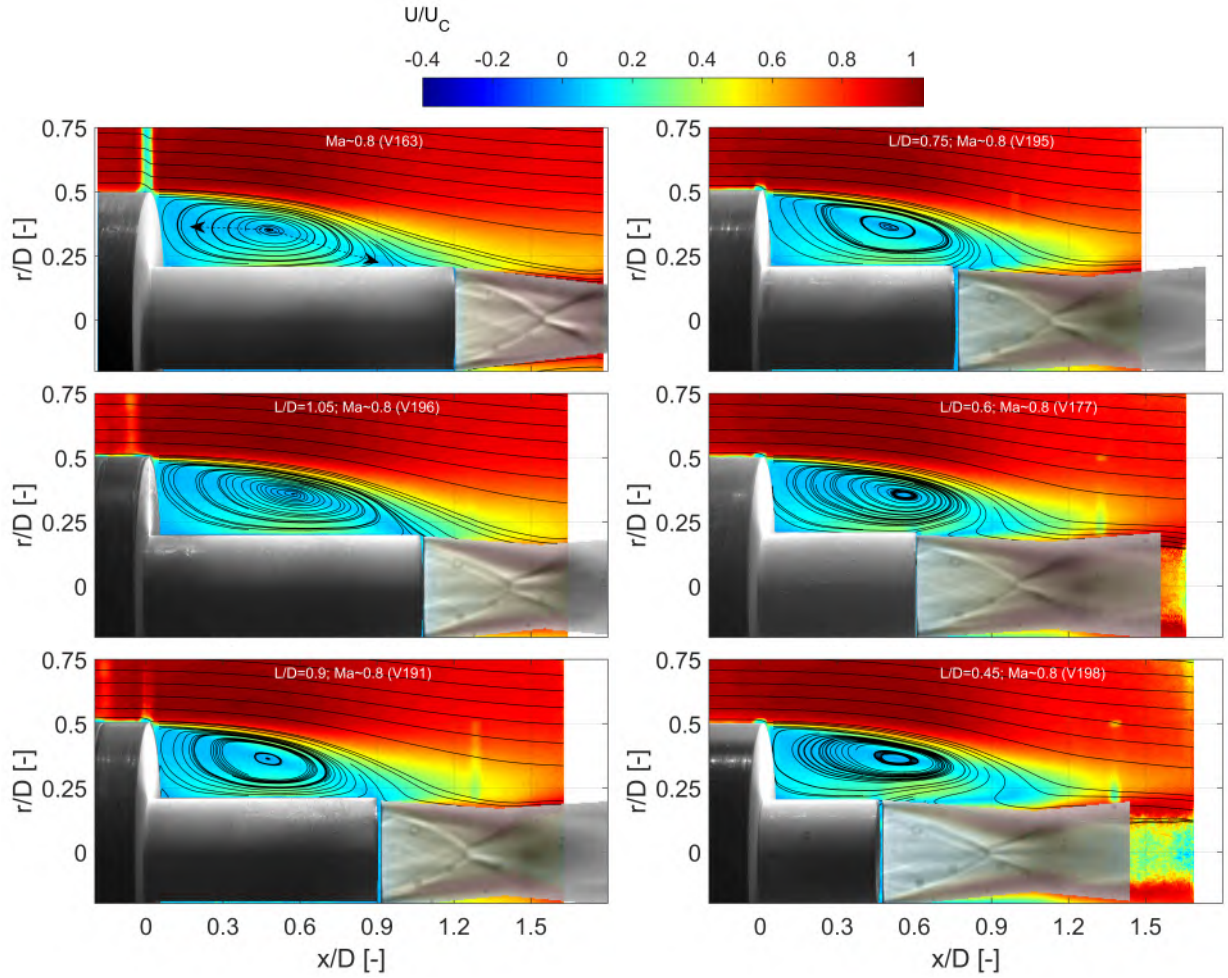

Figure 4: Velocity distribution with streamlines for the relative nozzle lengths $L/D = 1.2$, 1.05, 0.9, 0.75, 0.6 and 0.45.

3.2 Reynolds Stress Distribution

3.2.1 Axial Turbulence Intensity

The Saile et al. (2019a) has shown two regions as being highly turbulent. The first was attributed to the motion of the shear layer, which is commonly observed by all base flow investigations, and the second, to the 'dancing' motion of the large scale, clockwise rotating, coherent vortex. In the following description in the frame of Fig. 5, both regions are considered regarding the axial turbulence intensity content for the investigated nozzle lengths.

The remains of the 'dancing' vortex center are clearly visible (at $[(x,r)/D] = [0.57, 0.31]$) along the nozzle surface. The excitation in this region persists for the various shorter nozzle lengths, but the graphs

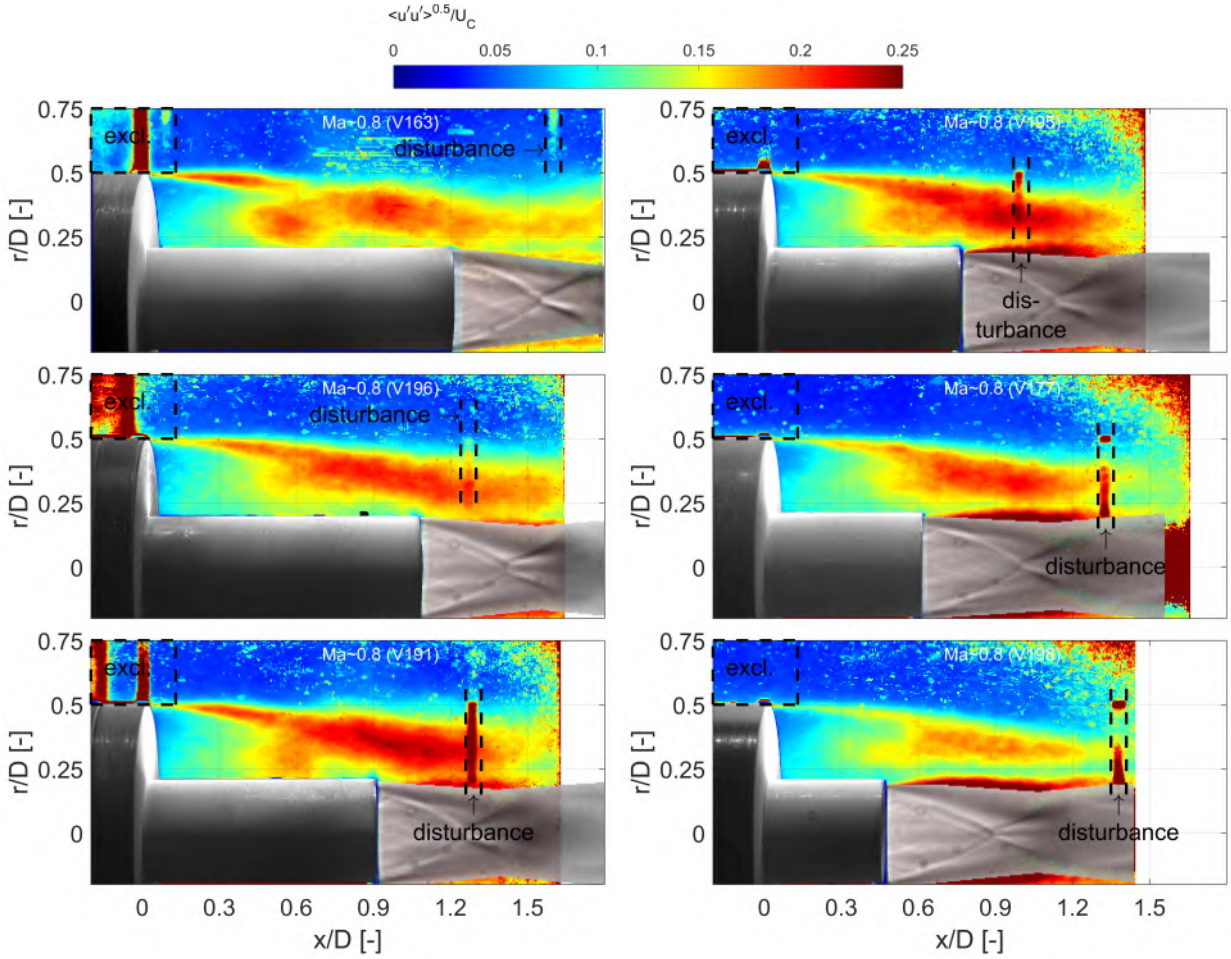

Figure 5: Normalized axial turbulence intensity distribution for the relative nozzle lengths $L/D = 1.2$, 1.05, 0.9, 0.75, 0.6 and 0.45.

do not reveal a clear dependency with respect to the nozzle length. For instance, an isolated and distinct excitation is notable for $L/D = 0.9$, but the distinctiveness disappears for the other nozzle lengths. There, the excitation from the shear layer is superimposed with the 'dancing' vortex center excitation, which obstructs a clear isolation of the two influences.

Generally, it can be stated that the shear layer excitation dominates. It increases with shorter nozzles, reaches a maximum for $L/D = 0.9$ and decreases again for even shorter nozzles. The evolution here points at the existence of a configuration which is most unfavorable regarding shear layer oscillations. This is a discussion point pursued in the coming sections.

3.2.2 Reynolds Shear Stress

The Reynolds shear stress distribution is depicted in Fig. 6. It is presented with the same intention as the axial turbulence intensity: To reveal regions of elevated turbulence with respect to their dependency on the nozzle length. These regions can predominantly be found along the operating range of the shear layer. There, the same tendency as for the turbulence intensity can be detected, meaning the level steadily increases up to a nozzle length $L/D = 0.9$, decreases from there for larger nozzle lengths before seemingly reaching a plateau. To quantify this behavior, the value at the 'center of gravity' of the 'island' with a Reynolds shear stress level above 95% of the maximum value is extracted and listed in Tab. 2. As further observation it can be stated that the effect of a 'dancing' main vortex center is less pronounced in the Reynolds shear stress distribution. Previous data presented in Saile et al. (2019a) already indicated that it predominantly affects the axial velocity fluctuations.

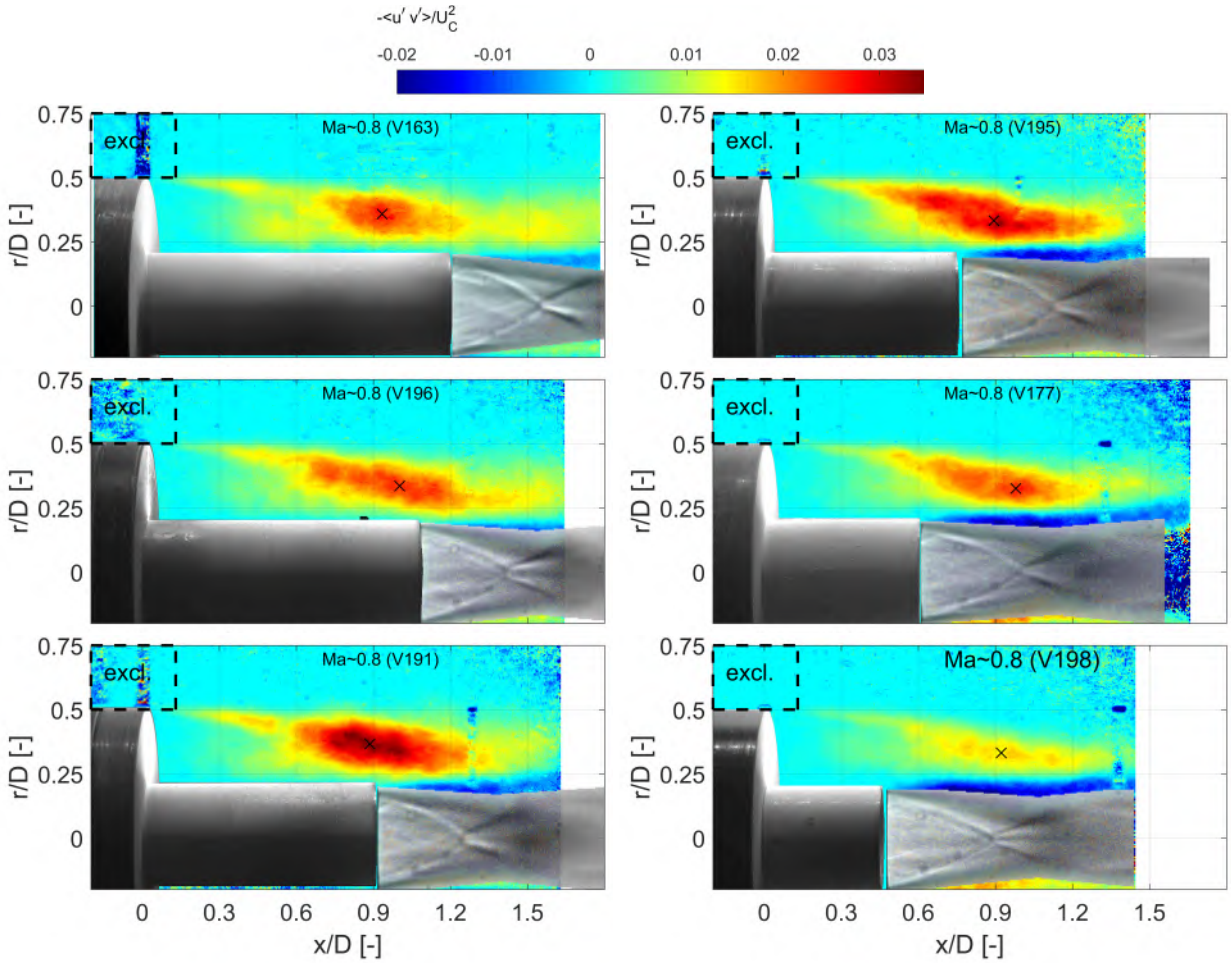

Figure 6: Normalized Reynolds stress distribution for the relative nozzle lengths $L/D = 1.2$, 1.05, 0.9, 0.75, 0.6 and 0.45. The crosses 'x' mark the locations of the Reynolds shear stress extraction for Fig. 8.

Table 2: The magnitude of the maximum Reynolds shear stress level $(u'v')_{max}/U_C^2$, its corresponding position $[(x,r)/D]^*$ and the position of the vortex center $[(x,r)/D]_{vc}$.

Run ID	L/D [-]	$[(x,r)/D]_{vc}$ [-]	$[(x,r)/D]^*$ $[ms^{-1}]$	$(u'v')_{max}/U_C^2$
V163	1.2	[0.48,0.35]	[0.93,0.36]	−0.0259
V196	1.05	[0.58,0.36]	[1.00,0.34]	−0.0249
V191	0.9	[0.47,0.36]	[0.89,0.37]	−0.0345
V195	0.75	[0.50,0.36]	[0.89,0.33]	−0.0304
V177	0.6	[0.56,0.36]	[0.98,0.33]	−0.0252
V198	0.45	[0.53,0.36]	[0.92,0.33]	−0.0138

3.3 Reynolds Stress related to the Nozzle Length

The previous trends regarding the turbulence intensity and Reynolds shear stress are now plotted in Fig. 7 as function of the relative nozzle length. The level for both is extracted from the point determined as maximum shear layer excitation (Tab. 2). The error bars are according to the 95% confidence interval as suggested by Benedict and Gould (1996) for the sampling uncertainty. The influence of the nozzle length for an axisymmetric configuration at Mach 0.76 with exhaust jet was also investigated by van Gent et al. (2017b) and the corresponding results are included.

Fig. 7 now depicts clearly the increase of maximum Reynolds shear stress level and the turbulence intensity location up to a nozzle length of 0.9. A further nozzle length increase seems to lead to a plateau at a lower turbulence level. This observation correlates with the finding that the excited area appears to shrink from a nozzle length of $L/D = 1.05$ to 1.2 (Fig. 6). In other words, it seems like the influence of the jet on the reattachment process decreases, ergo turbulent excitations reach a plateau, if the exhaust jet is placed at a location farther downstream.

Moreover, the current results also agree well with the findings by van Gent et al. (2017b). Please take into consideration that both results are based on experiments, meaning both results rely on the given setup and corresponding measurement uncertainties. In van Gent et al. (2017b), the wind tunnel model was supported by a strut and the experiments were performed in a closed wind tunnel. Nevertheless, the axial turbulent intensity is at a comparable level and it also features a maximal excitation for a nozzle length of $L/D = 0.9$. For a longer nozzle, the shear layer reattaches on the mean at $L_r/D = 1.1$, meaning the strongest excitation for that case is also reached if the configuration is as such that the mean shear layer reattachment takes place in the vicinity of the nozzle exit.

3.4 Particularities of the Amplified Excitation

The observation regarding the impact of changing the nozzle length could be of practical relevance for the design of space launcher systems. Obviously, the excitation of unsteady fluctuations in the base region is not desired. The reason for the differences regarding the level of excitation must be found in the investigated parameter space, which is the nozzle length only. That geometrical parameter is directly linked with the location of shear layer impingement relatively to the nozzle exit, and is consequently investigated more closely.

3.4.1 Probability Density Estimate

The impingement location of the shear layer is assessed by means of the probability density estimate of the axial velocity component just upstream from the nozzle exit. The corresponding function is shown in Fig. 8. Just upstream means $\Delta x/D = -0.01$ upstream from the individual nozzle exits at a radial distance of $r/D = 0.225$. The corresponding point is named P1 and is exemplarily depicted in the instantaneous velocity distribution plots below (Fig. 9, Fig. 10). In Fig. 8, the diamond symbol and the thin line represent the mean and median value, respectively.

Downstream pointing axial flow components are an indicator that reattachment takes place on the solid nozzle surface. This is predominantly the case for $L/D = 1.2$. Additionally, it was shown in the preceding study in Saile et al. (2019a) that this is the case where the shear layer starts interacting with the jet, which is at Mach 0.8. The current data provides another confirmation for this previously made observation: For $L/D = 1.05$, the axial flow component still points mostly in the downstream direction, but a significant share also points in the opposite direction. Then, for $L/D = 0.9$, the median shows that the ratio between upstream and downstream pointing axial velocity components is about equal. The tendency of diminishing downstream pointing flow components continues for the lower nozzle lengths until for $L/D = 0.6$ they become insignificant. In other words, the shear layer presumable does not reattach on the solid nozzle surface for $L/D \leq 0.6$. To conclude, the lowest excitations are found if the shear layer either completely overshoots the nozzle or if it only reattaches on the jet. Further, the strongest excitation is found if the shear layer reattaches on average at the tip of the nozzle.

3.4.2 Instantaneous Velocity Distribution

A temporary reattachment on the solid nozzle wall seems to be a common denominator for elevated turbulence levels in the base region. In the following, instantaneous velocity distributions are used to approach

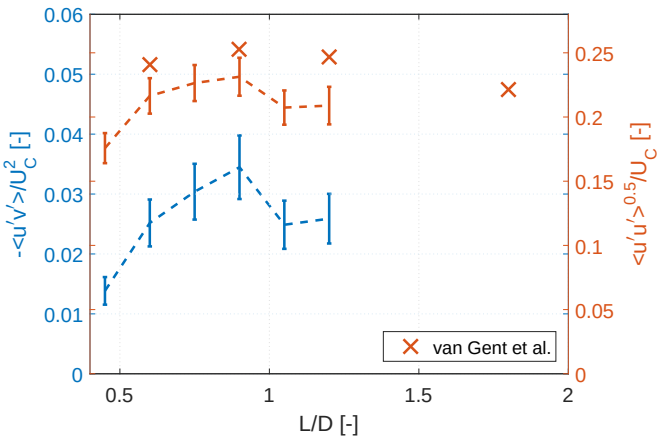

Figure 7: The turbulence intensity and Reynolds shear stress level in dependence of the relative nozzle length.

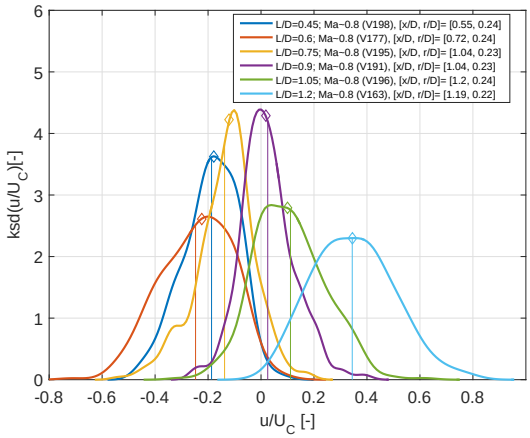

Figure 8: Probability density estimate PDF of the axial normalized velocity components sampled upstream from the nozzle exit at point P1. Diamond markers and thin continuous line denote the normalized mean and median axial velocity, respectively.

the causality behind that. Two instant scenarios of the configuration with a nozzle length of $L/D = 0.45$ are depicted as representative for the *low turbulence* case and three scenarios as representative for the *high turbulence* case. The latter concerns the configuration with a nozzle length of $L/D = 0.9$. The scenarios are chosen as such to reflect clear opposites in the spectrum of possible velocities at the point just upstream of the nozzle exit P1 as given in Fig. 8.

Keep in mind that those instantaneous velocity distribution plots of the $L/D = 1.2$ configuration were presented in Saile et al. (2019a) with the objective to identify the driver behind the high turbulence regions. One was attributed to the large-scale, clockwise rotation vortex and the other to the shear layer motion. With respect to the current considerations, it was found that the shear layer almost exclusively impinges on the solid nozzle wall (at Mach 0.8). In other words, the recirculation bubble is on the verge of interacting with the jet, but most of the time no connected interface between the two can be found. This configuration corresponds to one end of the spectrum.

The configuration with a nozzle length of $L/D = 0.45$ reflects the other end of the spectrum: The recirculation is not enclosed by the base and nozzle wall, but always exposed to the jet environment independent of the extent of the shear layer motion. The large-scale, clockwise rotating vortex is also visible for both *low turbulence* cases as shown in the graphs of Fig. 9. The top and bottom graphs depict an exemplary low and high axial velocity scenario ($u/U_C = -0.31$ and -0.01). On a first glance, the large scale flow features do not seem to be so different from what was observed for $L/D = 1.2$ in Saile et al. (2019a). For $L/D = 1.2$ though, the upstream traveling flow realigns along the nozzle surface. This is in contrast with at least one of the current scenarios: While the flow still realigns along the jet for the scenario $u/U_C = -0.31$, one can see that the flow is directly inhaled and ejected due to the jet for the other scenario. Farther downstream, mass appears to be ejected for both cases in the vicinity of $x/D = 0.9$. Further, both cases also indicate a mass engulfing process into the recirculation region as part of the large scale vortex.

The *high turbulence* case with $L/D = 0.9$ shown in Fig. 10 is in between the above described configurations. The graphs show three scenarios categorized by the direction and magnitude of the axial velocity just upstream from the nozzle exit. The axial velocity of the top, mid and bottom instance in time is positive ($u/U_C = 0.22$), close to zero (0.04) and negative (-0.23), respectively. By means of the low speed corridor (dark blue) or the vectors, one can recognize that shear layer reattachment takes place on the solid nozzle wall (top), right at the tip of the nozzle (mid) and on the jet (bottom). A further contrast to the previous results concerns the backwash due to the large, clockwise rotating vortex: The backwash runs along the solid nozzle wall and is not exposed to ejection effects by the jet. To put it more simply, the backwash is 'protected' from being inhaled and ejected by the jet.

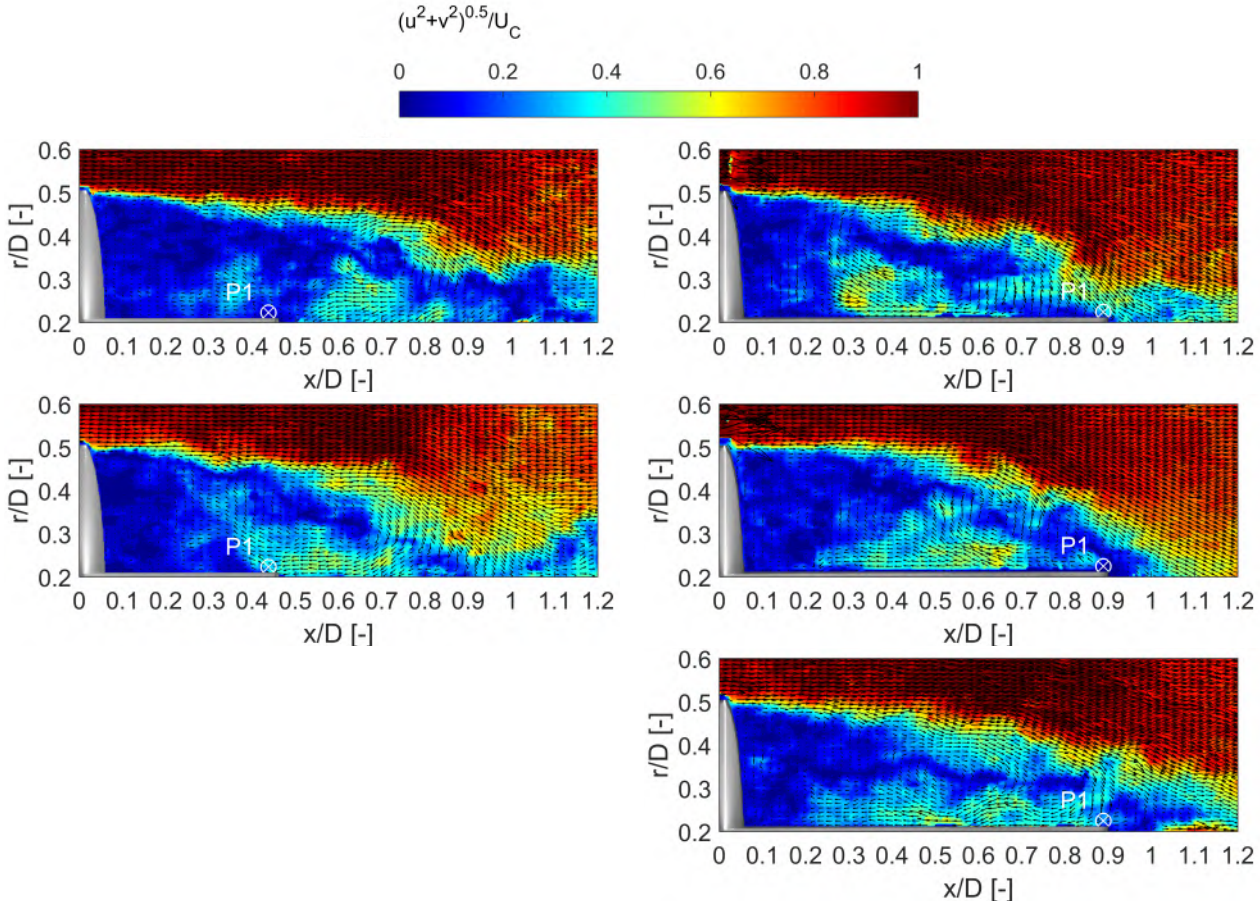

Figure 9: Instantaneous velocity distribution for the relative nozzle length of $L/D = 0.45$ with focus on point P1 just upstream from the nozzle exit. The top graph visualizes exemplarily a high axial velocity scenario ($u/U_C = -0.01$); the bottom graph a high reverse flow ($u/U_C = -0.31$) scenario. Every fourth and second vector is shown in x- and r-direction, respectively.

Figure 10: Instantaneous velocity distribution for the relative nozzle length of $L/D = 0.9$ to exemplarily visualize a positive ($u/U_C = 0.22$), close to zero (0.04) and negative axial velocity scenario (-0.23) at point P1 just upstream from the nozzle exit. Every fourth and second vector is shown in x- and r-direction, respectively.

3.5 Summarizing Discussion on the Near-Wake Flows of Various Base Geometries

The previous study Saile et al. (2019a) attributed the high turbulent intensity patches in the contour plot to either the 'dancing' vortex center of the large, counter-rotating vortex or to the shear layer motion. The current results also feature these intensified areas (Fig. 5) and due to the simililarities to the previous results it seems safe to assume that the origin of the excitation sources remain the same. The question now is: *What are the special conditions for the unwanted increased turbulent intensity region for the relative nozzle length of* 0.9 *(Fig. 7)?*

The PDF of the velocity samples just upstream of the nozzle exit (Fig. 8) reveal that the $L/D = 0.9$-case represents the configuration for which shear layer reattachment on the solid nozzle wall is equally frequent as on the exhaust jet. On the mean, the flow directly reattaches on the nozzle tip without flow reversal as for $L/D < 0.9$ and without impinging on the solid nozzle wall before as for > 0.9. This can also be seen by means of the low speed corridor and stagnation streamlines in the average velocity distribution (Fig. 4).

It appears that two criteria must be given for a maximal excitation: First (criterion 1), the mean recirculation bubble must be frequently connected with the jet. This idea is equal to the image of an open connection/interface between the base region and jet, or to the exclusion of the separated shear layer exclusively impinging on the solid nozzle wall. Under these circumstances, the results indicate that some dynamic exchange process is taking place, which in turn feeds turbulent excitations in the recirculation bubble. A symptom of which seems to be the 'dancing' main vortex center. Statnikov et al. (2017) suggested a *cross-pumping* motion where a vortical structure is shed from the main vortex every time the separation bubble is close to the nozzle exit. In fact, the POD of the current data set suggests as dominant POD mode such a vortex shedding process (addressed in Saile (2019)). Such a vortex shedding process essentially equals a mass loss from the base region. The jet is known to eject mass from the base region, which is also often called entrainment or base suction (e.g. Schoones and Bannink (1998); Deprés (2003); Wolf (2013)).

But, the turbulent excitation does not increase continuously with an increasing interface to the jet (or decreasing nozzle lengths). Consequently, there must be a second aspect, which introduces a dampening effect. The instantaneous velocity distributions for the relative nozzle length $L/D = 0.45$ (Fig. 9) show that the excitation decrease correlates with mass flow ejection from the large, clockwise rotating vortex. For the larger nozzle length $L/D = 0.9$ on the other hand (Fig. 10), the backwash induced by the vortex travels unhindered upstream along the solid nozzle wall. Thus, it appears that the excitation becomes maximal if the large, clockwise rotating vortex impinges on the nozzle wall only such that the complete energy and mass of that engulfing vortex is transferred to recirculation bubble. The description of the latter forms the second criterion (criterion 2).

It is hypothesized now that the $L/D = 0.9$ configuration at Mach 0.8 poses a scenario for which the vortex-shedding driven entrainment by the jet and mass supply by the engulfing large, clockwise vortex is maximal. Obviously, the design goal for a space launcher is the opposite: the minimization of dynamic processes and inherent base pressure fluctuations. Thus, the occurrence of such a circumstance should be avoided.

The plateau regarding the turbulent quantities for nozzle lengths larger than $L/D = 1.05$ (Fig. 7) is addressed as last point. It appears reasonable that a plateau is reached if reattachment predominantly takes place on the solid nozzle wall. Then the reattachment conditions are less and less influenced by the downstream environment. A predominant reattachment on the solid nozzle wall is found for a nozzle length $L/D \geq 1.05$ (Fig. 8). The region of increased Reynolds stresses is more confined for $L/D = 1.2$ in comparison to 1.05 (Fig. 5), which might be a consequence of a reduced base suction effect due to the increased distance from the entrainment source, ergo having a larger relative nozzle length.

4 Conclusions and Outlook

The research question of the current section considers *the impact of the base geometry*. Inherently, it revolves around the excitation mechanism of base flow that finally leads to buffet/buffeting for space launchers. The path of this section followed the traces of the preceding studies Saile et al. (2019b,a), which found for a space launcher configuration with a relative nozzle length of $L/D = 1.2$ at Mach 0.8 a limiting case: Under these conditions the near-wake/base flow starts to interact occasionally with the supersonic and over-expanded exhaust jet. The question now was what happens to the excitation, specifically to the Reynolds stresses, in the wake if the interaction is further enforced by decreasing the relative nozzle length. Correspondingly, this corresponds to a parametric study, which investigates the influence of the base geometry on the turbulent properties in the near-wake.

This question was approached experimentally by executing tests in the VMK on a wind tunnel model representing the base of a space launcher. The experiments here were exclusively executed at Mach 0.8 and at a Reynolds number of $1.4 \cdot 10^6$ for six different generic base geometries. The relative nozzle length has been enlarged by intervals of $\Delta L/D = 0.15$ from $L/D = 0.45$ to 1.2.

The main result concerns the existence of a presumably most unfavorable base geometry regarding the excitation of unsteady fluctuations in the base region. This is indicated for $L/D = 0.9$. For this configuration, upstream pointing velocity fluctuations are as frequent as downstream pointing fluctuations. It further corresponds to the configuration for which the reattachment on the mean does not take place along the solid nozzle wall, but just at the tip of the nozzle (without overhang). Moreover, it was hypothesized that an engulfment-entrainment process driven by a large-scale vortex and the jet is the driver for the relatively strong fluctuations. Consequently, it appears recommendable to avoid such a configuration due to its presumable impact as loads on the base structures of the space launcher.

In the future, it is planned to publish the results of the *proper orthogonal decomposition (POD)* analysis applied on the current data set to present the dominating motions in the base region. Data is available for various subsonic Mach numbers and for configurations with and without exhaust jet. The objective is to analyze the dependency of excited states to these parameters. Additionally, pressure data of the same configurations have been evaluated. Thus, a publication to show the spectral contents and periodic patterns is equally foreseen.

Acknowledgements

Financial support has been provided by the German Research Foundation (Deutsche Forschungsgemeinschaft - DFG) in the framework of the Sonderforschungsbereich Transregio 40. Further, thanks a lot to the colleagues and the staff for their support!

References

Benedict L and Gould R (1996) Towards Better Uncertainty Estimates for Turbulence Statistics. *Experiments in Fluids* 22:129–136

David S and Radulovic S (2005) Prediction of Buffet Loads on the Ariane 5 Afterbody. in *In 6th Symposium on Launcher Technologies, Munich, Germany, 8-11 November 2005*

Deck S and Thorigny P (2007) Unsteadiness of an Axisymmetric Separating-Reattaching Flow: Numerical Investigation. *Physics of Fluids* 19:065103

Deprés D (2003) *Analyse Physique et Modélisation des Instationnarités dans les Écoulements d'Arrière-Corps Transoniques*. Ph.D. thesis. Université de la Méditerranée Aix-Marseille II

Deprés D, Reijasse P, and Dussauge J (2004) Analysis of Unsteadiness in Afterbody Transonic Flows. *AIAA Journal* 42:2541–2550

DLR ACG (2019) Vertical Test Section Cologne (VMK), Supersonic and Hypersonic Technology Department

Fuchs H, Mercker E, and Michel U (1979) Large-Scale Coherent Structures in the Wake of Axisymmetric Bodies. *Journal of Fluid Mechanics* 93:185–207

Hannemann K, Ludeke H, Pallegoix JF, Ollivier A, Lambaré H, Maseland J, Geurts E, Frey M, Deck S, Schrijer F et al. (2011) Launch Vehicle Base Buffeting-Recent Experimental and Numerical Investigations. in *7th European Symposium on Aerothermodynamics*. volume 692. page 102

Lazar E, DeBlauw B, Glumac N, Dutton C, and Elliott G (2010) A Practical Approach to PIV Uncertainty Analysis. in *27th AIAA Aerodynamic Measurement Technology and Ground Testing Conference*. page 4355

Raffel M, Willert CE, Kompenhans J et al. (2007) *Particle Image Velocimetry: A Practical Guide*. Springer Science & Business Media

Saile D (2019) *Experimental Analysis on Near-Wake Flows of Space Transportation Systems*. Ph.D. thesis. submitted in February, 2019 at the Rheinisch-Westfälische Technische Hochschule Aachen

Saile D, Kühl V, and Gülhan A (2019a) On the Subsonic Near-Wake of a Space Launcher Configuration with Jet. *Experiments in Fluids (submitted and considered for publication)*

Saile D, Kirchheck D, Gülhan A, and Banuti D (2015) Design of a Hot Plume Interaction Facility at DLR Cologne. in *Proceedings of the 8th European Symposium on Aerothermodynamics for Space Vehicles*. 83419

Saile D, Kühl V, and Gülhan A (2019b) On the subsonic near-wake of a space launcher configuration without jet. *Experiments in Fluids* 60:50

Scharnowski S (2013) *Investigation of Turbulent Shear Flows with High Resolution PIV Methods*. Ph.D. thesis. Universität der Bundeswehr München, Fakultät für Luft- und Raumfahrttechnik

Scharnowski S, Bolgar I, and Kähler C (2016) Interaction of a Generic Space Launcher Wake with a Jet Plume in Sub-, Trans- and Supersonic Conditions. *International Workshop on Non-Intrusive Optical Flow Diagnostics*

Scharnowski S, Statnikov V, Meinke M, Schröder W, and Kähler CJ (2015) Combined Experimental and Numerical Investigation of a Transonic Space Launcher Wake. in *Progress in Flight Physics–Volume 7*. volume 7. pages 311–328. EDP Sciences

Schoones M and Bannink W (1998) Base Flow and Exhaust Plume Interaction. Part 1: Experimental study. *Series 01: Aerodynamics 15*

Schrijer F, Sciacchitano A, and Scarano F (2014) Spatio-Temporal and Modal Analysis of Unsteady Fluctuations in a High-Subsonic Base Flow. *Physics of Fluids* 26:086101

Schrijer F, Sciacchitano A, Scarrano F, Hannemann K, Pallegoix JF, Maseand J, and Schwane R (2011) Experimental Investigation of Base Flow Buffeting on the Ariane 5 Launcher using High Speed PIV. in *7th European Symposium on Aerothermodynamics*. volume 692. page 103

Schwane R (2015) Numerical Prediction and Experimental Validation of Unsteady Loads on Ariane 5 and Vega. *Journal of Spacecraft and Rockets*

Statnikov V, Bolgar I, Scharnowski S, Meinke M, Kähler C, and Schröder W (2016) Analysis of Characteristic Wake Flow Modes on a Generic Transonic Backward-Facing Step Configuration. *European Journal of Mechanics-B/Fluids* 59:124–134

Statnikov V, Meinke M, and Schröder W (2017) Reduced-Order Analysis of Buffet Flow of Space Launchers. *Journal of Fluid Mechanics* 815:1–25

Triesch K and Krohn EO (1986) *Die Vertikale Meßstrecke der DFVLR in Köln-Porz (Stand 1986), DFVLR-Mitt. 86-22*. Wissenschaftliches Berichtswesen der DFVLR, ISSN 0176-7739, Postfach 906058, 5000 Köln 90

van Gent P, Michaelis D, Van Oudheusden B, Weiss P, de Kat R, Laskari A, Jeon YJ, David L, Schanz D, Huhn F et al. (2017a) Comparative assessment of pressure field reconstructions from particle image velocimetry measurements and lagrangian particle tracking. *Experiments in Fluids* 58:33

van Gent P, Payanda Q, Brust S, van Oudheusden B, and Schrijer F (2017b) Experimental Study of the Effects of Exhaust Plume and Nozzle Length on Transonic and Supersonic Axisymmetric Base Flows. *7th European Conference For Aeronautics And Space Sciences*

Weiss P and Deck S (2013) Numerical Investigation of the Robustness of an Axisymmetric Separating/Reattaching Flow to an External Perturbation using ZDES. *Flow, Turbulence and Combustion* 91:697–715

Weiss P, Deck S, Robinet JC, and Sagaut P (2009) On the Dynamics of Axisymmetric Turbulent Separating/Reattaching Flows. *Physics of Fluids* 21:075103

Wolf CC (2013) *The Subsonic Near-Wake of Bluff Bodies*. Ph.D. thesis. Rheinisch-Westfälische Technische Hochschule Aachen, Fakultät für Maschinenwesen

Wong H, Meijer J, and Schwane R (2007) Experimental and Theoretical Investigation of Base-Flow Buffeting on Ariane5 Launch Vehicles. *Journal of Propulsion and Power* 23:116–122